

pubs.acs.org/JACS Article

# Surface Acidity of Oxygen Evolution Intermediates by Excited State Optical Spectroscopy

Michael Paolino, Suryansh Singh, Cassius Boyd, Moritz Lang, and Tanja Cuk\*



Cite This: J. Am. Chem. Soc. 2025, 147, 28474-28483



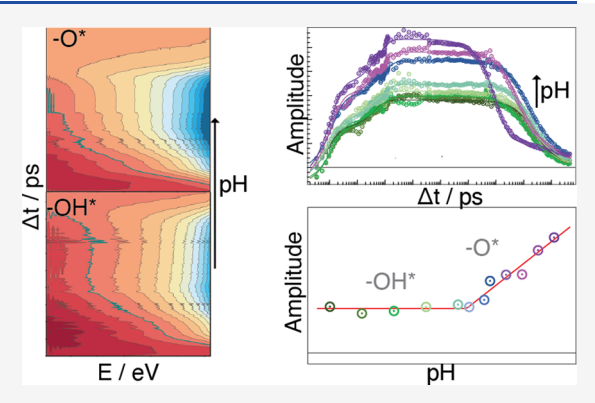
**ACCESS** I

III Metrics & More

Article Recommendations

s) Supporting Information

**ABSTRACT:** While the protonation of homogeneous metal-oxide catalysts is quite relevant for mechanisms in aqueous solution, the relevance of surface acidity to catalytic mechanisms of heterogeneous metal oxides is far less understood. Without a distinguishing metric ascribed to transient intermediates, invoking surface acidity is limited to rationalizing pH-dependent product evolution. Recently, the emissive population associated with intermediates of electron and proton transfer at a titanium oxide surface demonstrated an isotherm with pH whose half-rise occurred at pH = 11.8. As detected by a time-resolved visible broadband probe, the intermediates formed within <2 ps upon photoexcitation of the oxygen evolution reaction (OER) at an electron-doped (0.1% Nb) SrTiO<sub>3</sub>/ aqueous interface. Here, we demonstrate how the pH dependence of the <2 ps population is preserved such that when the intermediate population



finally decays with a time constant of 10  $\mu$ s, it does so with a pH onset at 11.4. The distinctive pH associated with a metastable population ascribes a surface acidity to the first intermediate of water oxidation, interpreted as favoring Ti–OH $^{\bullet}$  below and Ti–O $^{\bullet}$  above an acid dissociation constant (*i.e.*, p $K_a$ ). The work shows that the excited state optical spectroscopy is sensitive to protonation over the lifetime of metastable intermediates. Further, it shows that the details of the hydration layer prior to excitation are important for stabilizing intermediate populations of different acidities that then affect the chemical steps of water oxidation catalysis at longer time scales, *e.g.*, bond formation.

# INTRODUCTION

Half of the water splitting reaction that creates an energy storing fuel in the form of H<sub>2</sub> is the oxygen evolution reaction (OER) that involves four electron and two-proton transfers per O<sub>2</sub>. These are generally considered to occur as single proton-coupled electron transfer (PCET) reactions for which the metal—oxygen bond constrains the binding energies of reaction intermediates.<sup>1–3</sup> In principle, however, the acidity of the catalytic site and its environment can change the energetics of electron transfer out of the metal—oxygen bond,<sup>4</sup> which then defines different mechanistic regimes as a function of pH. Such effects can be important to better understand the molecular and chemical mechanism of OER.<sup>5,6</sup>

Thus, far, the role of acidity in the OER is the most well-defined for homogeneous catalysis. Electrochemistry of synthetically tailored molecules constructs mechanistic diagrams as a function of pH and electrode potential. For the most studied mononuclear homogeneous Ruthenium catalyst, in solution  $^{7,8}$  and attached to surfaces,  $^{9,10}$  regimes of pH and electrode potential exist for which reaction intermediates are created by electron transfer uncoupled to the proton transfer, by coupled two-electron, two-proton transfers, and by single electron transfers coupled to two-proton transfers.  $^{7}$  Separations between the regimes of PCET are related to an acid dissociation constant or  $pK_a$  of the electron transfer reaction

intermediates. More recently, electrochemistry of single-crystalline, epitaxial thin films of the 4d and 5d metallic oxides better defines the role of acidity in OER for heterogeneous catalysis. For RuO<sub>2</sub>, the binding energies of the first two PCET reaction intermediates depend on pH.<sup>11</sup>

Within heterogeneous catalysis, a challenge has been to quantify how acidity influences the OER on semiconducting metal-oxide surfaces. For (photo)-electrochemical OER on TiO<sub>2</sub>, pH dependencies have been observed on the populations and lifetimes of photoexcited intermediates. <sup>12–14</sup> However, the dependencies have not been quantified precisely enough across the range of relevant time scales to associate them with an equilibrium descriptor. There are several reasons to anticipate that the reaction intermediates and their binding energies depend on the acidity and protonation environment of the semiconducting catalyst surfaces. First, for noble metal TiO<sub>2</sub>, the electron transfers out of the water species and into

Received: June 13, 2025 Revised: July 10, 2025 Accepted: July 11, 2025 Published: July 28, 2025





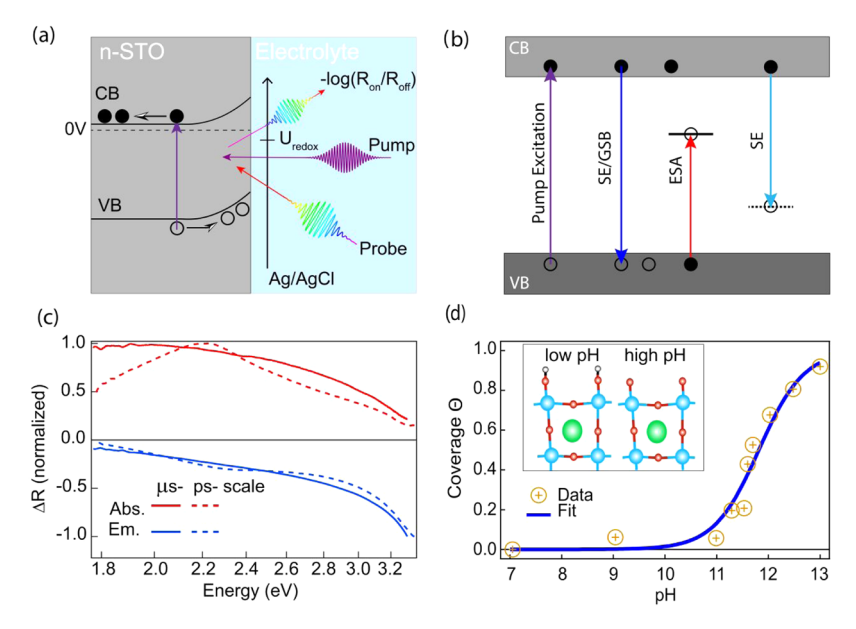


Figure 1. Excited state optical spectra at the STO/aqueous interface. (a) Schematic of the Schottky barrier at the 0.1% Nb STO/aqueous interface with 0 V vs Ag/AgCl applied to the back of the electrode. Above band gap photoexcitation (pump: 266 nm) leads to spontaneous OER probed by an ultrafast, broadband visible pulse (probe: 375–730 nm). (b) Energy level diagrams depicting emissive and absorptive transitions that contribute to the spectra in the visible range after band gap excitation. The bulk hole polaron state is shown as a dashed line. The corresponding transition is outside of our experimental range. (c) Normalized characteristic emissive and absorptive spectra from constrained SVD analysis at both pico- and microsecond time scales. (d) Langmuir isotherm derived from picosecond emissive population as a function of pH, suggesting a quasi-equilibrium constant for the excited state surface. Coverage  $\Theta = [\text{Ti-O}^{\bullet-}]/h_0^+$  where  $\text{Ti-O}^{\bullet-}$  denotes a particular chemical configuration of the trapped hole and  $h_0^+$  the total hole population. Adapted with permission from Nature Materials, 21, 88–94. Copyright 2022 Springer Nature. The inset is a schematic of surface protonation at low (<10) and high (>12) pH prior to photoexcitation.

the electrode—or, equivalently, a valence band edge hole transfer out of the electrode—have been associated with hole polarons for which distortions of neighboring Ti-O bonds localize charge onto surface oxygens. 15-17 Having such a local charge directly implies that surface acidity would play a role in the stability of PCET reaction intermediates. For example, the hole polaron configurations are calculated to be uniquely stable for hole-trapping on water species that have already been singly or doubly deprotonated. Further, O-H bond dissociation energies in PCET reactions are calculated to be significantly modified by the presence of hole and electron polarons. 18,19 Second, the early transition metal oxides are associated with a nonuniform hydration layer by both calculation and experiment; water dissociation leads to a heterogeneous distribution of adsorbed water species, hydroxyl groups, and fully deprotonated surface oxygens. 20-23 Each set of sites could influence the mechanism of the OER by allowing for differently protonated reaction intermediates, each with their unique binding energies. Finally, recent experimental work has identified pH 12 as distinctive for both hematite and strontium titanate; for hematite,<sup>24</sup> the interpretation is that the formation of the iron oxo (Fe=O) by electron transfer depends on the protonation of the surrounding solvent.

For strontium titanate, a scenario for which the proton configurations dictate the electron transfers has been recently advanced by experiments using an ultrafast and visible broadband probe of photoexcited (0.1% Nb) SrTiO<sub>3</sub> (STO). The excited state emission that forms within an ultrafast time scale of electron transfer (<2 ps) exhibits an isotherm with pH whose half-rise occurs at pH =  $11.8.^{25}$  However, identifying this pH dependence with an acid dissociation constant ( $pK_a$ ) implies that an equilibrium is reached on the excited state surface. Here, we show that the pH dependence originating at

ultrafast time scales is preserved through microseconds. Furthermore, the decay of the excited state populations to the subsequent reaction steps depends on a similar  $pK_a$ . The formation and decay kinetics are defined by two time constants each (1, 60, and 10  $\mu$ s, 100  $\mu$ s), with the 1 ps and 10  $\mu$ s populations exhibiting the pH dependence with an onset of pH = 11.8 and pH = 11.4, respectively. These populations are defined by the emission that has components at the band edge and below it. Assigning the excited state absorptive and emissive spectra to theoretically calculated optical dipoles of hole polarons is a challenge and a part of ongoing work. Here, we separate out the short-lived excited state absorption to focus on long-lived and pH-modulated emission.

The finding of a sharp pH dependence for intermediate populations metastable from ultrafast time scales on a heterogeneous metal oxide undergoing an OER identifies a surface  $pK_a$  that has so far characterized PCET for molecular catalysts. A mechanism based on Ti-OH and Ti-O reaction intermediates is proposed, whereby Ti-OH. intermediates form from water for pH prior to pK<sub>a</sub> and Ti-O<sup>•-</sup> intermediates form from hydroxyl groups for pH past the  $pK_a$ . Given that the hydration layer involves complex networks of hydrogen bonding at the solid-liquid interface,<sup>27</sup> these entities represent chemical rather than geometrical configurations. For example, the proton within Ti-OH is thought of as local not to a site but to the hydration layer. More generally, the work shows that excited state optical spectroscopy of heterogeneous metal-oxide surfaces, predominantly associated with electron transfer, is also quite sensitive to surface protonation.

# EXPERIMENTAL METHODS

Electrochemistry. 0.08% Nb-doped STOby weight (henceforth referred to as 0.1%) STO single crystals with the (100)-facet exposed to the electrolyte were obtained from MTI corporation. The thickness of the crystals was 0.5 mm, and the exposed side was polished (Ra < 5 Å). The rear face of the STO crystal is brought into electrical contact with a copper wire via a Gallium-Indium eutectic (Sigma-Aldrich, St. Louis, MO). The sample and wire are then covered with epoxy, followed by an insulating layer of liquid electrical tape, leaving the polished surface exposed. The sample is then mounted in a customdesigned cell, which holds the sample steady and accommodates an electrolyte solution along with a reference and counter electrode. The pH of the electrolyte solution is varied between 7 and 14 during experiments. Solutions below pH 14 were prepared using a phosphate buffer; the pH 14 solution was a 1 M solution of NaOH. An Ag/AgCl (3 M KCl) electrode was used as a reference, and a Pt wire served as a counter electrode (cathode). The potential was kept at 0 V throughout all experiments and was controlled by a CHI650E potentiostat (CH Instruments, Austin, TX) via the copper wire at the rear of the STO sample (anode). Sweeping this potential while monitoring the current through the sample amounts to a cyclic voltammetry measurement (Supplemental Figure S1A). This serves to clean the sample surface of contaminants and confirms a good electrical connection at the rear of the sample. Electrical current through the sample is monitored during data collection. This current is used to calculate the quantum efficiency of charge separation, as shown in Supplementary Figure S2.

Pump-Probe Spectroscopy. The OER catalytic cycle is timeresolved using pump-probe spectroscopy. The pump provides above band gap excitation, placing the SrTiO3 in an electronically excited state from which subsequent reaction steps are downhill. The system is then probed by a white light continuum pulse, which interrogates the newly formed OER intermediates on the SrTiO<sub>3</sub> surface through a change in reflectivity after pump excitation. The probe beam is derived from a regeneratively amplified Ti:sapphire laser system (Coherent Legend, Coherent Inc., Santa Clara, CA), which produces pulses with a center wavelength of 800 nm and pulse length of ca. 150 fs at a repetition rate of 1 kHz. Part of the amplifier output is directed into a CaF2 crystal to generate a white light continuum spanning from ca. 375-730 nm. The probe beam was directed onto the sample at a ca. 45° angle, which translates to a 32° angle of incidence on the sample itself after refraction through the cover glass and the electrolyte. (Supplemental Figure S1B,E). Two different pump sources are used to fully resolve the dynamics of our signal. Early time dynamics (short-time data, picosecond-nanosecond scale) are resolved using a fast (~500 fs) pump pulse generated from the third harmonic of the Coherent Legend output, with delays generated via a mechanical stage. Long-time dynamics (long-time data, ns- $\mu$ s scale) were studied using the 266 nm fourth harmonic output of an Innolas SpitLight Piccolo. The delay between the pump (Piccolo) and probe beams was adjusted by using a digital delay generator (SRSDG645, MenloPark, CA), where only every second trigger signal was used, resulting in a repetition rate of 500 Hz for the pump pulses. Raster scanning of the pump and probe across the sample surface is employed to prevent surface reconstruction from affecting the data. Information on these scanning methods and potential effects on data are shown in Supplemental Figure S3.

# RESULTS

Absorptive and Emissive Populations From Transient Reflectance. An ultrafast and visible broadband probe of the (0.1% Nb) STO/electrolyte interface tracks the excited state absorption, stimulated emission, and band-edge emission during the OER (Figure 1). Due to the well-defined Schottky barrier (Figure 1a), this interface was previously shown to have a high photon-to-current quantum efficiency (>70%) in a 3-electrode configuration with above band gap and ultrafast excitation (266 nm, 400 fs) and 0 V vs Ag/AgCl on the STO

working electrode (see Supplementary Figure S2).<sup>28</sup> The change in reflectivity is defined as  $\Delta R = -\log(R_{\rm on}/R_{\rm off})$ , where  $R_{\rm on}$  and  $R_{\rm off}$  are the measured intensities of the broadband reflected light with and without the pump excitation; in reflectivity, the pump-probe signals arise from a depth  $d \sim \lambda/$  $4\pi n_n^{29}$  where n is the real part of the refractive index and for the wavelengths  $\lambda$  probed d is 10–20 nm. Due to the high quantum efficiency during OER, a Schottky barrier of ~25 nm,<sup>28</sup> and the surface sensitivity of reflectance, the pumpinduced changes are associated with delocalized and trapped holes. The pump penetration depth d and the Schottky barrier W are shown in the diagram in Supplemental Figure S1C. Further, trapped electrons associated with occupied midgap states are not anticipated in Nb-doped STO due to the shallow Nb donor states<sup>30</sup> and the lack of a propensity to trap electrons in the form of Ti(III) in STO.<sup>31</sup> Emissive and absorptive signals arise due to excitations of electrons from the conduction and valence bands, respectively, to either unoccupied midgap states arising at a distorted reaction coordinate or band edge states at the equilibrium reaction coordinate (Figure 1b). If the excited state is due dominantly to a change in absorptivity (rather than a change in the real part of the polarization), a positive  $\Delta R$  corresponds to an excited state absorption (ESA, red), and a negative  $\Delta R$  signifies a ground-state bleach (GSB, blue) or a stimulated emission (SE, blue). Transient spectra can be decomposed into characteristic absorptive and emissive spectra<sup>25</sup> (Figure 1c), allowing for separate analysis of their contributions to the data. Both contain spectral weight well below the band gap (3.2 eV), for which there is little ground-state absorption; Supplementary Figure S1D shows the real and imaginary refractive indices for STO.

In this article, data are taken during the OER to focus on the population dynamics of long-lived hole states. In particular, the focus will be on a long range of metastability between the picosecond and microsecond time scales found for the emission. Spectrally, the below band gap emission is associated with bulk hole polarons, stable in STO; a prominent spontaneous emission peak near 2.5 eV is seen in photoluminescence, which theoretical calculations have assigned to bulk hole polarons<sup>32,33</sup> (Figure 1b). In our data, a near-bandedge emission is present, which is also seen in some photoluminescence studies through the band edge<sup>34,35</sup> (Figure 1c). There could be multiple origins of the near-band-edge emission that arise from either excited state populations of the ground-state electronic levels or changes in the conduction and valence band states due to photoexcitation. The most usual assignment is a ground-state bleach of the electronic levels due to electron, hole occupation of the valence, and conduction bands, respectively. However, the population dynamics associated with this excited state configuration are those of electron-hole recombination. For STO, recombination dynamics measured by a near-band-edge pump excitation (to highlight bulk, delocalized carriers) exhibits a ~60 ns lifetime and can be modeled by band-to-band auger recombination processes as a function of photocarrier intensity.<sup>36</sup> The metastability over a wide range of time scales encompassing the nanosecond regime suggests that this near-band-edge emission originates from new stable states. Further, the emissive spectrum, inclusive of the midgap and near-band edge regions, consistently tracks a similar metastable population modulated by circuit conditions<sup>28</sup> (open, closed) and the electrolyte<sup>25</sup> (pH), which also suggests that it probes

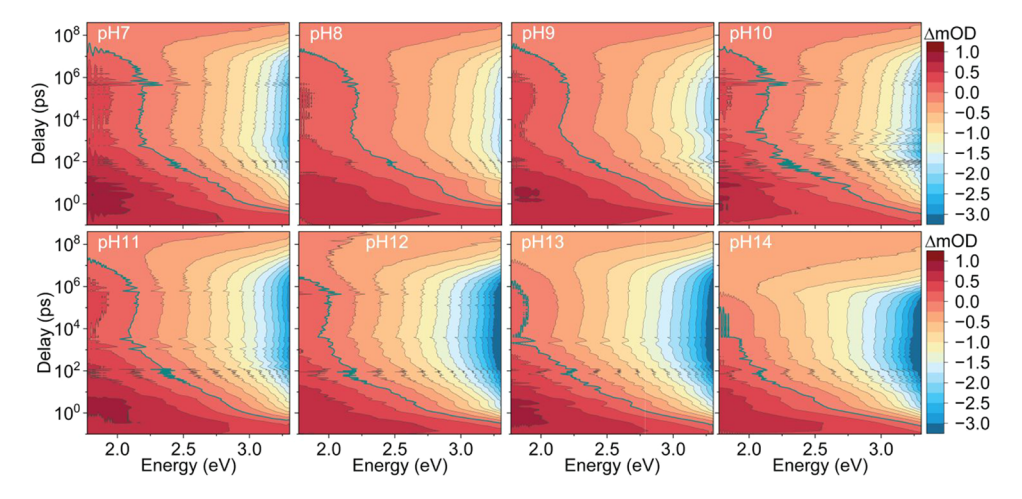


Figure 2. Time—energy contour plots of absorptive and emissive signals for pH 7–14. Contour plots of concatenated data were reconstructed from the first 2 SVD components for each pH data point. Each pH point shows time-dependent absorptive (red) and emissive (blue) optical transitions. The green line highlights the zero-contour line. The absorptive signature fully develops within ~1 ps and decays within ~100 ps. The emissive signature grows more slowly (~100 ps) and remains metastable out to the microseconds and fully decays only by ~100  $\mu$ s. The magnitude of the absorptive signature is not sensitive to pH, whereas the emissive signature increases markedly past pH 11.

long-lived hole states whose population is subject to external conditions.

One of the unique properties of the metastable emission is that it describes an intermediate population with a sharp pH dependence between 11 and 12. The pH-dependent population arises from ultrafast emissive growth. This was shown in a recent manuscript<sup>25</sup> using a principal component analysis<sup>37</sup> whose emissive and absorptive spectrum for the <1 ns range is reproduced in Figure 1c, along with that of the spectra for the microsecond data reported here. The pH dependence of the picosecond emissive population is shown in Figure 1d (baseline corrected using pH 7). The dependence saturates at higher pH and is therefore modeled with a surfacelimited Langmuir isotherm as a function of pH with a half-rise of pH 11.8. Since this isotherm is for the excited state surface formed within a of couple picoseconds, it is a composite of the ground-state equilibrium of the surface with the bulk electrolyte prior to photoexcitation and the metastable equilibrium upon photoexcitation. Cartooned in Figure 1d are changes to the protonation of the hydration layer with pH prior to excitation, which we come back to in the discussion.

Ultrafast Formation, Metastability, and Decay of pH-Dependent Emission. Transient spectra of the n-doped STO/electrolyte interface, showing the entire lifetime of the emissive population, were collected at pH values ranging from 7 to 14. To view the dynamics of these transient spectra over their entire lifetime, data must be collected on two separate time scales. Ultrafast dynamics at the early time scale (short-time) are resolved using finely spaced delays in the range of 0–4 ns. The remainder of the dynamics (long-time) are captured using delays in the range of 1 ns–500 μs. Time-resolved spectra were achieved by concatenation of short- and long-time scale data sets, using the short-time scale transient spectra (Supplementary Figure S4) as a benchmark.

The resulting concatenated transient spectra shown in Figure 2 are achieved by a linear scaling of the long-time data, calculated by a comparison of spectra from short- and long-time scale data (Supplementary Figure SS) at common delays. A comparison of spectra at the point of concatenation is used to establish a common zero crossing point (Supplementary Figure S6). Scaling factors, which minimize the

difference between spectra for each common delay (Supplementary Figure S7), are then used to determine a single factor for the long-time data, at each pH point.

The resulting contour plots allow for the rise, metastability, and decay of the absorptive (positive OD, pink-red) and emissive (negative OD, orange-blue) signals to be viewed simultaneously (Figure 2). The absorptive contribution occurs for the lower energy range of the broadband probe, decays after 100s of ps, and does not show a distinctive pH dependence. The emissive contribution occurs in the highenergy region of the broadband probe and shows a distinct pH dependence. This emission develops within the first ~100 ps, remains metastable on the nanosecond scale, and ultimately decays on the microsecond scale. The pH dependence is reflected in the magnitude of the emission on the nanosecond scale. Between pH 7 and 10, the emission is independent of pH. Beginning near pH 11, the emission increases, as shown by the higher energy range of the broadband probe (2.8–3.2 eV) and by a changing zero-contour line (green) as the emission increasingly reduces the overlapping absorption. The microsecond kinetics also displays a dependence on pH; the emission at pH 14 decays to zero faster.

For a more quantitative analysis of the emissive population dynamics, constrained singular value decomposition (SVD) analysis is performed on the concatenated data (Supplementary Figures S8-S11). SVD analysis reveals two dominant spectral components that represent the transient data, as indicated by the relative magnitude of the singular values (Supplementary Figure S8). These spectral components can be constrained such that there is one purely absorptive and one purely emissive spectral component representing poles of the imaginary refractive index in optical spectroscopy (Supplemental Figure S9). Constraining the spectra amounts to choosing a basis and is achieved by manually tuning parameters that shift the spectra at each pH (Supplemental Figure S10). Kinetics have a positive sign by convention and represent the relative magnitudes of the corresponding emissive and absorptive populations at each pH. When the different pH conditions are represented with common spectral components, the corresponding kinetic components confirm that the absorptive portion of the spectrum is fairly pH-

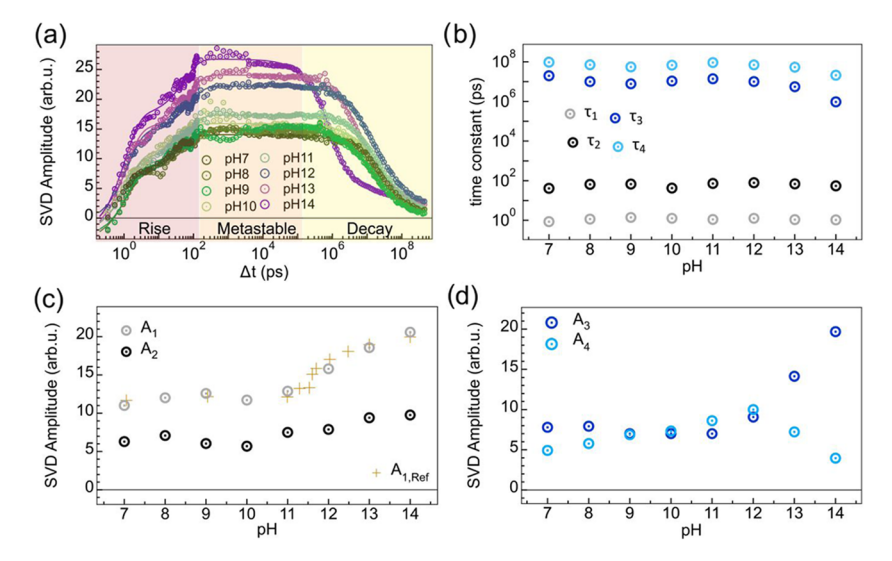


Figure 3. Emissive population dynamics from picoseconds to microseconds and its pH dependence. (a) SVD kinetics (circled dots) and fits of concatenated data (solid lines). Kinetics were normalized by integrating the corresponding absorptive kinetics for each pH point and then fit with a 4-exponential function. Regions are shaded to highlight the rise, metastability, and decay of the emissive populations. (b) Exponential time constants obtained from the fits. The rising portion of the signal is defined by 2 distinct time constants (gray circles  $\tau_1$ , black circles  $\tau_2$ ), and the decaying portion is defined by 2 distinct time constants (light blue circles  $\tau_3$ , dark blue circles  $\tau_4$ ). (c) Amplitudes of the fast (gray circles,  $A_1$ ) and slow (black circles,  $A_2$ ) rising components, representative of their relative populations. The fast rise emissive population carries a pH dependence with an onset between pH 11 and 12. Included is the pH dependence reproduced from the previously published ultrafast data (dark yellow crosses,  $A_{1,ref}$ ) shown in Figure 1c. This data was scaled and offset to match the absolute values of  $A_1$  and allow for a visual comparison; adapted with permission from Nature Materials, 21, 88–94. Copyright 2022 Springer Nature. (d) Amplitudes of the fast (light blue circles,  $A_3$ ) and slow (dark blue circles,  $A_4$ ) decaying components, representative of their relative populations. The fast-decaying population carries a pH dependence with an onset past pH 11.

independent and that the bulk of the pH dependence is carried by the emissive population dynamics (Supplementary Figure S11). The common emissive and absorptive spectra across the full time and pH ranges of the concatenated data are shown in Figure 1c.

Figure 3a shows the pH-dependent emissive kinetics for the concatenated data set; these kinetics are normalized to the integrated absorption at each pH to account for changes in fluence and pump-probe overlap during data collection. The presence of two separate time constants on the rising edge of the data was demonstrated in our previous publication.<sup>25</sup> Similarly, two exponential components are required to reproduce the decay of the kinetics. This can be interpreted as the rise and decay of two distinct populations. Such a model results in a kinetic function with two amplitudes  $A_1$  and  $A_2$ , each associated with one rise and one decay time constant (eq S13). Comparing this model with one that assumes four independent populations, thus placing fewer constraints on the data, noticeably favors the model with four amplitudes (Chapter 6 in the Supporting Information). Especially at longer delay times in the microsecond range, this favorability is quantifiable by looking at the fit errors. The two-amplitude model results in a fit error up to eight times higher than the four-amplitude model at high pH. This suggests a more complex process than the simple case of two separate and independent populations. To quantify the pH dependence, the emissive SVD kinetics are therefore fit with the 4-exponential function:

$$S(t) = A_1 \cdot \left[ 1 - \exp\left(-\frac{t}{\tau_1}\right) \right] + A_2 \cdot \left[ 1 - \exp\left(-\frac{t}{\tau_2}\right) \right]$$

$$+ A_3 \cdot \exp\left(-\frac{t}{\tau_3}\right) + A_4 \cdot \exp\left(-\frac{t}{\tau_4}\right) + C$$
(1)

This model contains two rising exponentials, two decaying exponentials, and a constant offset accounting for background fluctuations in the data and any pump-probe signals beyond the time window. For all pH conditions, four distinct time constants  $\tau_n$  (Figure 3b) with corresponding amplitudes  $A_n$ (Figure 3c,3d) were obtained. For the two rising exponentials, the fit results reveal a fast  $(\tau_1 \approx 1 \text{ ps})$  and a slow  $(\tau_2 \approx 60 \text{ ps})$ rising time constant, both of which are constant across all measured pH. The corresponding amplitudes represent the relative populations of fast  $A_1$  and a slow  $A_2$  growing emissive species. The pH dependence on the growth amplitudes is carried by the fast (1 ps) growth amplitude  $A_1$  (gray circles, Figure 3c) while the slow (60 ps) growth amplitude  $A_2$  remains relatively constant across pH (black circles, Figure 3c). We note that  $A_1$  used for the Langmuir isotherm in the previous work was collected with six pH points between pH 11 and 12, while the data here are sparser, with a point at each pH.<sup>25</sup> These previous ultrafast data points (yellow crosses, Figure 3c) are plotted along with the concatenated data (gray circles, Figure 3c).

The microsecond decay is fit by a fast ( $\tau_3 \approx 10~\mu s$ ) and slow ( $\tau_4 \approx 100~\mu s$ ) decay constant. The decay constants  $\tau_3$  and  $\tau_4$  decrease toward higher pH (Figure 3b). The bulk of the pH dependence for the microsecond decay lies in the fast decay amplitude  $A_3$  (Figure 3d). The slow decay amplitude  $A_4$  remains relatively constant across pH. Altogether, several characteristics of the population dynamics extracted from the

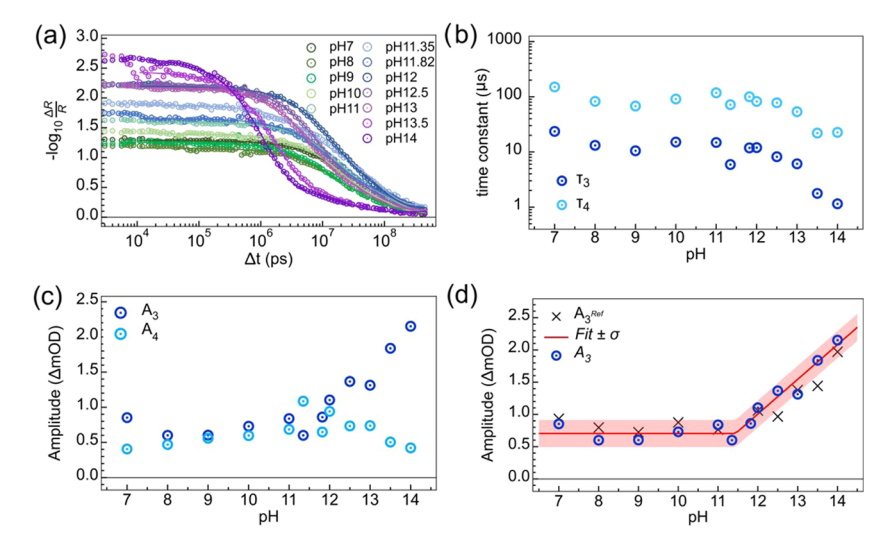


Figure 4. Quantifying microsecond emissive population dynamics as a function of pH. (a) Time traces at 3.1 eV (circles) at various pH and corresponding fits (lines) of averaged long-time data using eq 2. (b) Microsecond exponential decay time constants obtained from the fits (dark blue circles  $\tau_3$ , light blue circles  $\tau_4$ ). (c) Amplitude of microsecond populations from the fits (dark blue circles  $\Lambda_4$ ) light blue circles  $\Lambda_4$ ). (d) Amplitude of the fast-decaying population ( $\Lambda_3$ ) of the averaged data shown in part (a). The pH dependence is fit by eq 3, a constant and linear rising function. The estimated error (shaded red) is shown with respect to the fit (red line), as described in the text. The onset (pH0) is found to be at ca. pH 11.4. Black crosses ( $\Lambda_3$  ref) are the amplitudes of the fast-decaying component when the data is not averaged while controlling for beam power and stability as described in the text.

SVD kinetics are preserved from the picosecond rise to the microsecond decay: (1) Both regions are defined by two distinct time constants, one fast and one slow, across all pH. (2) The pH dependence of the emission in both regions is carried by the population associated with the faster time constant. (3) The pH dependence has a distinct onset after pH 11.

**Excited State p** $K_a$  by the Metastable Emissive Population. We now focus on quantifying the pH dependence of the microsecond emission. The fitting of concatenated data with a single equation means that the behavior of the kinetics in the short-time region has an influence over the fit parameters in the long-time region ( $A_3$  and  $A_4$ ). Data concatenation itself also scales the long-time data, which can impact the fit results. By focusing on the microsecond regime, we can also collect finally spaced pH points, which are needed to quantify the onset beyond pH 11.

Data collection at the long-time scale requires the use of an electronically triggered laser system. Though this laser system is excellent at producing pulses at irregular intervals (varying delays), it does suffer from energy and Poynting instabilities. Short-term instabilities can be easily accounted for, but long-term instabilities (hours to days) are more challenging to correct. We have addressed this problem in two different ways: (1) Collecting multiple repeats ( $\geq$ 4) of long-time data for each pH point, which are then averaged. (2) Collecting long-time data sets consisting of all pH points in a single day, while controlling for beam size and power between each data set (see Supporting Information chapter 7).

The results for the kinetic traces using the averaged data at each pH are listed in Figure 4a. Analyzing each single time trace first and then averaging the results has no effect on the outcome. This is discussed in more detail in Chapter 7 of the Supporting Information. Since the absorption has almost completely decayed by the beginning of the long-time scale (1 ns) data, the dynamics of the transient spectrum in this region can be described in whole by the emission. SVD analysis of the

long-time spectra (Supplementary Figure S17) reveals one significant principal component, whose spectrum is nearly all emissive. This allows for direct analysis of the long-time data through the raw kinetics of the transient spectrum at a single wavelength in the emissive region, 400 nm (3.1 eV) plotted in Figure 4a for each pH. The 3.1 eV long-time kinetic traces are fit by

$$S(t) = A_3 \cdot \exp\left(-\frac{t}{\tau_3}\right) + A_4 \cdot \exp\left(-\frac{t}{\tau_4}\right) + C \tag{2}$$

The resulting curve fits are plotted on the kinetic traces of Figure 4a. The fit results for all parameters are listed in Table S2. The decay time constants  $\tau_n$  and the extracted amplitudes  $A_n$  are plotted in Figure 4b,4c as a function of pH. Consistent with concatenated data, the 2-exponential fit reveals two distinct time constants, one fast  $(\tau_3 \approx 10 \ \mu s)$  and one slow  $(\tau_4)$  $\approx$  100  $\mu$ s) across all measured pH. As observed with the concatenated data, there is little to no population pH dependence prior to pH 11, and the pH dependence that onsets after pH 11 is carried by the fast decay population  $A_3$ . The long-time data show that a clear pH dependence on both  $\tau_3$  and  $\tau_4$  exists, with  $\tau_3$  and  $\tau_4$  constants decreasing past pH 12 (Figure 4b). Since the decrease of  $\tau_4$  also occurs in the fouramplitude model of the concatenated data but not in the twoamplitude model, the separate fits of the long-time data favor the four-amplitude model (Chapter 6 in the Supporting Information).

The pH dependence carried by population  $A_3$  is quantified in Figure 4d. A piecewise linear function, constant for pH < pH0 with a linear increase for pH > pH0, was chosen to establish a pH onset (pH0)

$$A_3(\text{pH, pH0, }A_0, m)$$
  
=  $A_0 \cdot \theta(-\text{pH + pH0}) + (m \cdot (\text{pH - pH0}) + A_0) \cdot \theta(\text{pH - pH0})$  (3)

It is important to establish an uncertainty in this model beyond that of the fit itself. To achieve this, eq 2 was fitted to the kinetics at 3.1 eV for each repeat of the long-time data set at each pH. The resulting  $A_3$  populations at each pH are then averaged, and a standard deviation for each pH is calculated. The averages are plotted as blue circles in Figure 4d and fit by eq 3; the fit is shown as a red line. The uncertainty in the fit for  $A_3$  vs pH (red shaded area in Figure 4d) is taken to be the standard deviation of the data with respect to the fit to eq 3. The standard deviation of ca. 0.21 mOD reported here is the average standard deviation across all pH points (Supplementary Figure S16 and Table S1). The fit yields an onset pH of ca. 11.4 and a rise of ca. 0.49 mOD/pH. The black crosses in Figure 4d represent fast decay amplitudes from the data set collected in a single day with rigid control over beam size and power between each pH point. This method of data collection serves to minimize long-time variance at the expense of signalto-noise due to a smaller data set. The points follow the same trend as the highly averaged data, confirming that the trend is independent of a longer-term laser instability.

## DISCUSSION

The pH dependence observed for the transient populations on  $SrTiO_3$  during the OER associates a fast picosecond rise to a microsecond decay, with a long range of metastability in between. Further, the pH dependence is quantified to be between 11 and 12 using a Langmuir isotherm for the 1 ps population (pH = 11.8) and a linear onset for the 10  $\mu$ s population (pH = 11.4). These results—the similar and quantifiable pH onset in very different time regimes along with the region of metastability—suggest that an acid equilibrium dissociation constant (p $K_a$ ) exists for intermediate populations of the OER in this pH range.

Such a  $pK_a$  for intermediate species of the OER has often been observed for molecular, homogeneous catalysts, categorizing regimes of electron and proton transfer as a function of pH and potential in Pourbaix diagrams. An example is the 2.9 pK<sub>a</sub> of the one-electron transfer intermediate [Ru(III)-OH<sub>2</sub>]<sup>3+</sup> for the mononuclear Ru catalyst.<sup>7</sup> At an In<sub>2</sub>O<sub>3</sub> surface, electron transfer rates to the attached Ru catalyst are found to be pH-dependent, identifying competing PCET pathways. 9,10 For these homogeneous catalysts, a  $pK_a$  is ascertained by electrochemical voltammetry; breaks in the Nernstian dependence of -59 mV/pH and regions of pH independence identify the pK<sub>a</sub>. For wide band gap semiconductors, surface protonation modulated by the electrolyte pH has been well documented by how the band edge potentials move with ca.  $-59 \text{ mV/pH.}^{38}$  While in the semiconductor literature, the Nernstian dependence is often associated with proton transfers alone, thermodynamically, the dependence could equally be associated with a series of single proton and electron transfer couples.<sup>39</sup> In either case, since the band potentials are measured rather than the potential of an intermediate species, the Nernstian dependence represents an average across many sites, each with its own acidity. Supplemental Figure S18 shows the Nernstian dependence for Nb-doped SrTiO3 with a somewhat smaller slope (-45 mV/pH), which could indicate that surface acidity plays a role. There is a leveling off at a higher pH that could be associated with a  $pK_a$ , but it is not pronounced.

Here, we advance an interpretation of the results based on a  $pK_a$  of the transient intermediate species isolated by photoexcitation and the emissive spectra. The closest analogy is

pulse radiolysis, which initiates reactions with high-energy pulses from an accelerator, isolates populations spectrally, and quantifies their pH dependence to regularly assign  $pK_a$ 's to intermediate species of electron transfer, especially in aqueous solutions.  $^{40-43}$  In this interpretation, the extracted emissive population counts the total number of one-electron intermediates or equivalently, hole polarons.<sup>44</sup> The similarity in the emissive spectra at picosecond and microsecond time scales (Figure 1c) and the metastable kinetics (Figure 3a) suggest that a trapped population is counted independently of its geometric configuration or protonation. The single electron transfer required for one-electron intermediates is justified by (1) the picosecond time scale of the ultrafast pH dependence, (2) the relatively low fluence used in the experiments (0.04 mJ/cm<sup>2</sup>) equivalent to 2% of surface sites, <sup>28</sup> and (3) a saturation in the emissive signal with higher fluence corresponding to an equivalent of 5% of surface sites.<sup>21</sup>

One way to understand an increase in the emissive population after pH 11 is that an additional driving force for hole-trapping becomes relevant at pH > p $K_a$  of the intermediate. This is an underlying assumption for the Langmuir isotherm model in the prior manuscript.<sup>25</sup> Here, a difference in free energy for intermediate formation between the hydroxyl (Ti-OH•) and oxyl (Ti-O•-) radicals is invoked without attempting to model the detailed isotherm(s) of Figures 3 and 4. The Ti-OH is presumed to occur from initially hydroxylated sites, while Ti-O<sup>•-</sup> is presumed to occur from fully deprotonated sites; given the simplified nature of the reactions and a heterogeneous hydration layer, the protonation of the intermediate only refers to whether a proton has left to the bulk electrolyte. In other words,  $Ti-OH^{\bullet}$  could occur in many different configurations, with the proton in the dangling configuration or bound to neighboring surface sites either directly or by H-bonds. We use the following reactions for Ti-OH and Ti-O

$$Ti - OH_2 \leftrightarrow Ti - OH^{\bullet} + H^{+} + e^{-} \text{ with } \Delta G_{OH^{\bullet}}$$
 (4)

$$Ti - OH^- \leftrightarrow Ti - O^{\bullet-} + H^+ + e^- \text{ with } \Delta G_{O^{\bullet-}}$$
 (5)

In the above, the VB hole is written as a product electron from the reactant on the surface into the valence band; this presumes that the electrochemical potential at which the electron transfer occurs is near the valence band edge. The free energies  $\Delta G_{\mathrm{OH}}^{\bullet}$  and  $\Delta G_{\mathrm{O}}^{\bullet-}$  associated with reactions 4 and 5 are the result of PCET reactions, which could occur either sequentially or concertedly. In the sequential case, the proton transfer occurs prior to photoexcitation (either as a pure proton transfer or coupled to an electron transfer), while the valence band electron transfer occurs after photoexcitation. In the concerted case, the proton transfer and valence band electron transfer both occur after photoexcitation. In either case, however, the thermodynamics of the reactions should be the same.<sup>39</sup>  $\Delta G_{OH}^{\bullet}$ , in particular, can be thought of as the O-H bond dissociation free energy of an absorbed water molecule, which has been calculated for the shown configuration Ti-OH<sub>2</sub><sup>15</sup> and for the dissociative one Ti-OH<sup>-</sup>H<sup>+18</sup> on rutile TiO<sub>2</sub>. The bond dissociation energies are quite high (~100 kcal/mol or 4.3 eV) and not unlike that used to create a hydroxyl radical from water. In a recent work that involves some of the same authors, the free energy of the electron transfer from Ti-OH- to the VB hole has been calculated for both rutile TiO<sub>2</sub> and STO; for both titanium

oxides, the free energies are spontaneous and large compared to the thermal bath.  $^{26}$ 

The thermodynamics of the conversion between  $Ti - OH^{\bullet}$  and  $Ti-O^{\bullet-}$  can be considered either on the ground-state surface prior to electron transfer or on the excited state surface after the electron transfer. On the excited state surface, the following reaction is used

$${
m Ti}-{
m OH}^{ullet} 
ightarrow {
m Ti}-{
m O}^{ullet^-}+{
m H}^++{
m e}^- \quad {
m with} \ \Delta G_{{
m O}^{ullet^-}/{
m OH}^{ullet}} \eqno(6)$$

The acid dissociation constant of this reaction differentiates the energetics of the PCET for reaction 4 from that of reaction 5. As shown in Supplemental Section 10, one can write the formation free energy of reaction 5 in terms of the formation free energies of (4) and (6)

$$\Delta G_{\mathrm{O}^{\bullet-}} = \Delta G_{\mathrm{OH}^{\bullet}} + \Delta G_{\mathrm{O}^{\bullet-}/\mathrm{OH}^{\bullet}} \tag{7}$$

Equation 7 is derived by first summing Reaction 4 and 5 and then replacing  $Ti-OH_2$  by its equilibrium with  $Ti-OH^- + H^+$ . With this recasting,  $Ti-O^{\bullet-}$  formation from valence band holes requires an additional, proton-related formation free energy compared to  $Ti-OH^{\bullet}$  formation. In the data, the emission is constant prior to pH 11, which this interpretation suggests is due to Reaction 4 being spontaneous and reaching completion (of the product side) already at pH 7. The increase of emission is then ascribed to Reaction 5 becoming spontaneous only after pH 11, given the additional free energy required by  $\Delta G_{O^{\bullet-}/OH^{\bullet}}$  (Reaction 6).

Some of the assumptions that go into this interpretation can be justified by calculated and experimentally measured  $pK_a$ values. First, the deprotonation of an adsorbed water site (Ti-OH<sub>2</sub>) to create a hydroxylated one (Ti-OH<sup>-</sup>) has a calculated  $pK_a$  7–9,<sup>20</sup> albeit for a rutile TiO<sub>2</sub> structure. With this  $pK_a$  for Ti-OH-, Ti-OH formation by Reaction 4 would reach completion already in the near-neutral region. We note that in the prior manuscript for the ultrafast data, 25 only Reaction 4 was invoked. Given the range of the relevant  $pK_a$  for titanium oxide and the fact that the data do not show a change nearneutral pH, Reaction 5 is likely more appropriate. Reaction 6 has been measured by pulse radiolysis to have a p $K_a$  of 11.8, <sup>42</sup> which is very close to what is obtained for the ultrafast isotherm and in the range of the onset of the microsecond isotherm. For this  $pK_a$ , the additional free energy needed for proton transfer at pH = 0,  $\Delta G_{O}^{\bullet-}/OH^{\bullet}$  is 0.68 eV. Since the electron transfer events in the pulse radiolysis experiments arise from exciting bulk water, making a connection between them and the STO electrode assumes that the Ti sites are spectators in the reaction. That Ti is a spectator is also suggested by: 1) the neutral pH range for deprotonation of a water-absorbed site which identifies equal parts hydroxyl and protons as in bulk water, and 2) the Ti(IV) ground state configuration is preserved upon hole-trapping as identified by the calculations described above that create Ti (IV)-OH\* from p-band VB holes<sup>15,18,26,39</sup>

In addition to the thermodynamic reasoning given above, a full kinetic modeling of the mechanism that patterns the time-dependent emission is desired. There are several difficulties in defining this kinetic modeling, which would yield time-dependent coverages of Ti–OH<sup>•</sup> and Ti–O<sup>•</sup>. The first is that the protonation of the surface hydration layer prior to excitation is understood to differentiate the coverages (Figure 1d) rather than a proton transfer on the excited state surface. The sample equilibrates with the bulk electrolyte prior to

photoexcitation, and the initial formation of the intermediates is ultrafast. Further, we did not observe an H/D isotope effect on the formation of the emissive signal, which would be anticipated for a population that strongly depends on proton transfer occurring on the excited state surface.<sup>25</sup> While metal oxides have been quantified for their hydration layer at nearneutral conditions by ambient pressure XPS, doing so as a function of pH has proved challenging experimentally.<sup>23,45-47</sup> Thus, the starting conditions required for the kinetic model are not well-defined. Second, the data shows biexponential rises and decays, which means that, in principle, four populations are tracked. While modeling using only two populations can fit the data, such that the pH dependence of one population is connected from ultrafast to microsecond time scales, this constraint is hard to justify without other experimental or theoretical input. Most of the pH dependence might be carried by a single population, but exchanges with the less pHdependent population in the region of metastability would significantly change the kinetic models. Evidence of this exchange is in the decay time constants, which both exhibit a pH dependence when four populations are tracked (Figure 4b) while the rising time constants are largely pH-independent. The exchange is especially relevant in the case in which the pH dependence is truly linear for the 10  $\mu$ s population (Figure 4d), while it saturates for the 1 ps population (Figure 3c). Finally, the band gap emission is not specific to a surface hole polaron configuration, such that the spectra themselves cannot differentiate between the protonation of different intermediate populations.

While a full kinetic model would better inform catalytic mechanisms, thermodynamics alone can provide some insights into improving efficiencies by catalyst design. The availability of Ti-O\*- intermediates after pH 11 and the fact that they seem to be additive to the Ti-OH suggest that at the higher pH, there are more sites for oxygen evolution created by the initial electron transfer. So, at a given overpotential, there would be more OER current at pH 11-14—which is reflected in the detailed pH dependence of our prior STO studies.<sup>25</sup> It also suggests that there are additional pathways for chemical bond formation that could result from the initial electron transfer at higher pH. The O-O chemical bond could occur, in principle, as a result of two Ti-OH coupling, two Ti-O -coupling, or cross-coupling between Ti-OH and Ti-O -. Since the microsecond time constants decrease beyond pH 11, one could argue that they reflect changes in how the O-O bond formation occurs mechanistically and that it occurs faster with the availability of one-electron transfer intermediates of different acidity. Overall, the metastability of these oneelectron intermediates through microsecond time scales suggests that after initiating the first electron transfer, the rest of the reaction steps are spontaneous (as also predicted by theory<sup>3</sup>). Altogether, these insights suggest that designing more efficient titanium oxide catalysts involves tuning the electrophilicity of the hydration layer such that both hydroxyl and oxyl radicals can be created at a range of pH conditions. While this is not entirely surprising, these time-resolved experiments motivate more detailed attention to be paid to such synthetic strategies. Since there are changes associated with OER intermediates on semiconducting iron oxides at pH  $12^{24}$  and the explanation here relates the surface p $K_a$  to hydroxyl and oxyl radicals created from bulk water, the strategies could be general for the early transition metal oxides.

#### CONCLUSIONS

Three regimes of a picosecond rise, nanosecond metastability, and microsecond decay are observed for the dynamics of an excited optical emission that is prominent when the SrTiO<sub>3</sub>/ aqueous interface is undergoing efficient, photodriven oxygen evolution catalysis. While previous work has associated the midgap and near-band gap transitions with trapped holes on oxygen sites, one missing and defining feature for such an assignment is the nanosecond metastability isolated here that connects ultrafast electron transfer processes with microsecond time scales associated with chemical bonding. Together with the metastability, the distinctive pH dependence of the emission now established across the full time range—with a half-rise at pH 11.8 for the 1 ps population and an onset at pH 11.4 for the 10  $\mu$ s population—identifies an acid dissociation constant as being relevant to the creation of one-electron intermediates on an oxide surface. Given previously calculated and measured  $pK_a$ 's for oxygen radicals and titanium oxide surfaces, an interpretation is advanced, whereby Ti-OH form from water for pH prior to the p $K_a$  and Ti-O $^{\bullet-}$  form from hydroxyl groups for pH past the  $pK_a$ . The finding of a  $pK_a$  for intermediate populations that has so far characterized protonassisted electron transfer for homogeneous, mononuclear catalysts is unique for a heterogeneous metal oxide and advances our understanding of the electron and proton transfers that can occur to generate reactive intermediates of oxygen evolution.

# ASSOCIATED CONTENT

# Supporting Information

The Supporting Information is available free of charge at https://pubs.acs.org/doi/10.1021/jacs.5c10001.

> Description of electrochemical sample cell setup, including representative cyclic voltammograms, diagram of the sample cell, band diagram of n-STO/electrolyte interface, ellipsometry data, and cartoon of transient reflectance geometry; steady-state current measurements, averaged current, and quantum efficiency as a function of pH; justification and description of step scanning of STO samples during data collection; details for the concatenation of data sets; an overview of SVD and its' use in analyzing concatenated data sets; amplitudes and time constants from alternative fit function; long-time data set fitting for singles repeats and averages of repeats; SVD analysis of long-time data sets; changes to the band edge with pH and RHE scale; and a description of free energies for the first and second proton transfer from a hydrated surface (PDF)

#### AUTHOR INFORMATION

# **Corresponding Author**

Tanja Cuk - Department of Chemistry and Renewable and Sustainable Energy Institute (RASEI) and Renewable and Sustainable Energy Institute (RASEI), University of Colorado, Boulder, Colorado 80303, United States; orcid.org/0000-0002-1635-2946; Email: tanja.cuk@ colorado.edu

# **Authors**

Michael Paolino - Department of Physics and Renewable and Sustainable Energy Institute (RASEI), University of Colorado, Boulder, Colorado 80303, United States

Suryansh Singh – Materials and Science Engineering Program and Renewable and Sustainable Energy Institute (RASEI), University of Colorado, Boulder, Colorado 80303, United States

Cassius Boyd – Department of Chemistry and Renewable and Sustainable Energy Institute (RASEI), University of Colorado, Boulder, Colorado 80303, United States; orcid.org/0000-0003-1533-919X

Moritz Lang - Renewable and Sustainable Energy Institute (RASEI), University of Colorado, Boulder, Colorado 80303, United States

Complete contact information is available at: https://pubs.acs.org/10.1021/jacs.5c10001

#### **Notes**

The authors declare no competing financial interest.

## ACKNOWLEDGMENTS

This work was supported by the Director, Office of Science, Office of Basic Energy Sciences, and by the Division of Chemical Sciences, Geosciences and Biosciences of the U.S. Department of Energy at RASEI (Boulder, CO) under Contract No. DE-SC0018939.

# REFERENCES

- (1) Hammer, B.; Norskov, J. K.Theoretical surface science and catalysis--calculations and concepts. In Advances in Catalysis, 2000; Vol. 45, pp 71-129.
- (2) Man, I. C.; Su, H.-Y.; Calle-Vallejo, F.; Hansen, H. A.; Martínez, J. I.; Inoglu, N. G.; Kitchin, J.; Jaramillo, T. F.; Nørskov, J. K.; Rossmeisl, J. Universality in Oxygen Evolution Electrocatalysis on Oxide Surfaces. ChemCatChem 2011, 3 (7), 1159-1165.
- (3) Rossmeisl, J.; Qu, Z. W.; Zhu, H.; Kroes, G. J.; Nørskov, J. K. Electrolysis of water on oxide surfaces. J. Electroanal. Chem. 2007, 607 (1-2), 83-89.
- (4) Hammes-Schiffer, S.; Stuchebrukhov, A. A. Theory of Coupled Electron and Proton Transfer Reactions. Chem. Rev. 2010, 110 (12), 6939-6960.
- (5) Seh, Z. W.; Kibsgaard, J.; Dickens, C. F.; Chorkendorff, I.; Norskov, J. K.; Jaramillo, T. F. Combining theory and experiment in electrocatalysis: Insights into materials design. Science 2017, 355 (6321), eaad4998 DOI: 10.1126/science.aad4998.
- (6) Busch, M.; Halck, N. B.; Kramm, U. I.; Siahrostami, S.; Krtil, P.; Rossmeisl, J. Beyond the top of the volcano? - A unified approach to electrocatalytic oxygen reduction and oxygen evolution. Nano Energy 2016, 29, 126-135.
- (7) Polyansky, D. E.; Muckerman, J. T.; Rochford, J.; Zong, R.; Thummel, R. P.; Fujita, E. Water Oxidation by a Mononuclear Ruthenium Catalyst: Characterization of the Intermediates. J. Am. Chem. Soc. 2011, 133 (37), 14649-14665.
- (8) Concepcion, J. J.; Tsai, M.-K.; Muckerman, J. T.; Meyer, T. J. Mechanism of Water Oxidation by Single-Site Ruthenium Complex Catalysts. J. Am. Chem. Soc. 2010, 132 (5), 1545-1557.
- (9) Cui, K.; Soudackov, A. V.; Kessinger, M. C.; Xu, J.; Meyer, G. J.; Hammes-Schiffer, S. General Kinetic Model for pH Dependence of Proton-Coupled Electron Transfer: Application to an Electrochemical Water Oxidation System. J. Am. Chem. Soc. 2023, 145 (35), 19321-
- (10) Kessinger, M.; Soudackov, A. V.; Schneider, J.; Bangle, R. E.; Hammes-Schiffer, S.; Meyer, G. J. Reorganization Energies for Interfacial Proton-Coupled Electron Transfer to a Water Oxidation Catalyst. J. Am. Chem. Soc. 2022, 144 (44), 20514-20524.
- (11) Kuo, D.-Y.; Paik, H.; Kloppenburg, J.; Faeth, B.; Shen, K. M.; Schlom, D. G.; Hautier, G.; Suntivich, J. Measurements of Oxygen Electroadsorption Energies and Oxygen Evolution Reaction on

- RuO2(110): A Discussion of the Sabatier Principle and Its Role in Electrocatalysis. J. Am. Chem. Soc. 2018, 140 (50), 17597–17605.
- (12) Imanishi, A.; Okamura, T.; Ohashi, N.; Nakamura, R.; Nakato, Y. Mechanism of Water Photooxidation Reaction at Atomically Flat TiO2 (Rutile) (110) and (100) Surfaces: Dependence on Solution pH. J. Am. Chem. Soc. 2007, 129 (37), 11569–11578.
- (13) Kafizas, A.; Ma, Y.; Pastor, E.; Pendlebury, S. R.; Mesa, C.; Francàs, L.; Le Formal, F.; Noor, N.; Ling, M.; Sotelo-Vazquez, C.; Carmalt, C. J.; Parkin, I. P.; Durrant, J. R. Water Oxidation Kinetics of Accumulated Holes on the Surface of a TiO2 Photoanode: A Rate Law Analysis. ACS Catal. 2017, 7 (7), 4896–4903.
- (14) Chen, X.; Aschaffenburg, D. J.; Cuk, T. Selecting between two transition states by which water oxidation intermediates decay on an oxide surface. *Nat. Catal.* **2019**, *2* (9), 820–827.
- (15) Cheng, J.; VandeVondele, J.; Sprik, M. Identifying Trapped Electronic Holes at the Aqueous TiO2 Interface. *J. Phys. Chem. C* **2014**, *118* (10), 5437–5444.
- (16) Chen, J.; Li, Y. F.; Sit, P.; Selloni, A. Chemical Dynamics of the First Proton-Coupled Electron Transfer of Water Oxidation on TiO2 Anatase. *J. Am. Chem. Soc.* **2013**, *135* (50), 18774–18777.
- (17) Di Valentin, C.; Selloni, A. Bulk and Surface Polarons in Photoexcited Anatase TiO2. *J. Phys. Chem. Lett.* **2011**, 2 (17), 2223–2228.
- (18) Warburton, R. E.; Mayer, J. M.; Hammes-Schiffer, S. Proton-Coupled Defects Impact O—H Bond Dissociation Free Energies on Metal Oxide Surfaces. *J. Phys. Chem. Lett.* **2021**, *12* (40), 9761–9767.
- (19) Warburton, R. E.; Soudackov, A. V.; Hammes-Schiffer, S. Interfacial Proton-Coupled Electron Transfer via Localized Trap States on Metal Oxide Surfaces. *J. Phys. Chem. C* **2024**, *128* (19), 7903–7912.
- (20) Cheng, J.; Sprik, M. Acidity of the Aqueous Rutile TiO2(110) Surface from Density Functional Theory Based Molecular Dynamics. *J. Chem. Theory Comput.* **2010**, *6* (3), 880–889.
- (21) Holmström, E.; Spijker, P.; Foster, A. S. The interface of SrTiO3 and H2O from density functional theory molecular dynamics. *Proc. R. Soc. A* **2016**, 472 (2193), 20160293.
- (22) Aschaffenburg, D. J.; Kawasaki, S.; Pemmaraju, C. D.; Cuk, T. Accuracy in Resolving the First Hydration Layer on a Transition-Metal Oxide Surface: Experiment (AP-XPS) and Theory. *J. Phys. Chem. C* **2020**, *124*, 21407 DOI: 10.1021/acs.jpcc.0c05195.
- (23) Ketteler, G.; Yamamoto, S.; Bluhm, H.; Andersson, K.; Starr, D. E.; Ogletree, D. F.; Ogasawara, H.; Nilsson, A.; Salmeron, M. The nature of water nucleation sites on TiO2(110) surfaces revealed by ambient pressure X-ray photoelectron spectroscopy. *J. Phys. Chem. C* **2007**, *111* (23), 8278–8282.
- (24) Liu, Y.; Le Formal, F.; Boudoire, F.; Guijarro, N. Hematite Photoanodes for Solar Water Splitting: A Detailed Spectroelectrochemical Analysis on the pH-Dependent Performance. ACS Applied Energy Mater. 2019, 2 (9), 6825–6833.
- (25) Vinogradov, I.; Singh, S.; Lyle, H.; Paolino, M.; Mandal, A.; Rossmeisl, J.; Cuk, T. Free energy difference to create the M-OH\* intermediate of the oxygen evolution reaction by time-resolved optical spectroscopy. *Nat. Mater.* **2022**, *21* (1), 88–94.
- (26) Boyd, C.; McBride, S.; Paolino, M.; Lang, M.; Hautier, G.; Cuk, T. Assigning Surface Hole Polaron Configurations of Titanium Oxide Materials to Excited-State Optical Absorptions. *J. Am. Chem. Soc.* **2025**, *147*, 10981 DOI: 10.1021/jacs.4c15043.
- (27) Gonella, G.; Backus, E. H. G.; Nagata, Y.; Bonthuis, D. J.; Loche, P.; Schlaich, A.; Netz, R. R.; Kühnle, A.; McCrum, I. T.; Koper, M. T. M.; Wolf, M.; Winter, B.; Meijer, G.; Campen, R. K.; Bonn, M. Water at charged interfaces. *Nat. Rev. Chem.* **2021**, 5 (7), 466–485.
- (28) Cuk, T.; Paolino, M.; Singh, S.; Stewart, J.; Chen, X.; Vinogradov, I. Ultrafast Electronic and Vibrational Spectroscopy of Electrochemical Transformations on a Metal-Oxide Surface during Oxygen Evolution Catalysis. ACS Catal. 2024, 14 (13), 9901–9926.
- (29) Sabbah, A. J.; Riffe, D. M. Femtosecond pump-probe reflectivity study of silicon carrier dynamics. *Phys. Rev. B* **2002**, *66* (16), No. 165217.

- (30) Osorio-Guillén, J.; Lany, S.; Zunger, A. Atomic Control of Conductivity Versus Ferromagnetism in Wide-Gap Oxides Via Selective Doping: V, Nb, Ta in Anatase \${\mathrm{TiO}}\_{2}\$. *Phys. Rev. Lett.* **2008**, *100* (3), No. 036601.
- (31) Chambers, S. A.; Droubay, T. C.; Capan, C.; Sun, G. Y. Unintentional F doping of SrTiO3(001) etched in HF acid-structure and electronic properties. *Surf. Sci.* **2012**, *606* (3), 554–558.
- (32) Rubano, A.; Paparo, D.; Granozio, F. M.; Scotti di Uccio, U.; Marrucci, L. Blue luminescence of SrTiO3 under intense optical excitation *J. Appl. Phys.* 2009; Vol. 106 10 DOI: 10.1063/1.3256140.
- (33) Janotti, A.; Varley, J. B.; Choi, M.; Van de Walle, C. G. Vacancies and small polarons in SrTiO<sub>3</sub>. *Phys. Rev. B* **2014**, 90 (8), No. 085202.
- (34) Yamada, Y.; Kanemitsu, Y. Band-to-band photoluminescence in \$\{\text{SrTiO}}\_{3}\\$. *Phys. Rev. B* **2010**, 82 (12), No. 121103.
- (35) Mochizuki, S.; Fujishiro, F.; Minami, S. Photoluminescence and reversible photo-induced spectral change of SrTiO3. *J. Phys.: Condens. Matter* **2005**, *17* (6), 923–948.
- (36) Yamada, Y.; Yasuda, H.; Tayagaki, T.; Kanemitsu, Y. Photocarrier recombination dynamics in highly excited SrTiO3 studied by transient absorption and photoluminescence spectroscopy *Appl. Phys. Lett.* 2009; Vol. 95 12 DOI: 10.1063/1.3238269.
- (37) Cuk, T. Phenomenology of Intermediate Molecular Dynamics at Metal-Oxide Interfaces. *Annu. Rev. Phys. Chem.* **2024**, *75* (75), 457–481.
- (38) Xu, Y.; Schoonen, M. A. A. The absolute energy positions of conduction and valence bands of selected semiconducting minerals. *Am. Mineral.* **2000**, *85* (3–4), 543–556.
- (39) Mayer, J. M. Bonds over Electrons: Proton Coupled Electron Transfer at Solid-Solution Interfaces. J. Am. Chem. Soc. 2023, 145 (13), 7050-7064.
- (40) Rabani, J.; Matheson, M. S. Pulse Radiolytic Determination of pK for Hydroxyl Ionic Dissociation in Water. *J. Am. Chem. Soc.* **1964**, 86 (15), 3175–3176.
- (41) Rabani, J.; Mulac, W. A.; Matheson, M. S. The Pulse Radiolysis of Aqueous Tetranitromethane.1 I. Rate Constants and the Extinction Coefficient of eaq-. II. Oxygenated Solutions. *J. Phys. Chem. A* **1965**, 69 (1), 53–70.
- (42) Weeks, J. L.; Rabani, J. The Pulse Radiolysis of Deaerated Aqueous Carbonate Solutions. I. Transient Optical Spectrum and Mechanism. II. pK for OH Radicals1. *J. Phys. Chem. A* **1966**, 70 (7), 2100–2106.
- (43) Grills, D. C.; Polyansky, D. E.; Fujita, E. Application of Pulse Radiolysis to Mechanistic Investigations of Catalysis Relevant to Artificial Photosynthesis. *ChemSusChem* **2017**, *10* (22), 4359–4373.
- (44) Singh, S.; Lyle, H.; D'Amario, L.; Magnano, E.; Vinogradov, I.; Cuk, T. Coherent Acoustic Interferometry during the Photodriven Oxygen Evolution Reaction Associates Strain Fields with the Reactive Oxygen Intermediate (Ti-OH\*). *J. Am. Chem. Soc.* **2021**, *143* (39), 15984–15997.
- (45) Marshall, M. S. J.; Newell, D. T.; Payne, D. J.; Egdell, R. G.; Castell, M. R., Atomic and electronic surface structures of dopants in oxides: STM and XPS of Nb- and La-doped SrTiO3(001). *Phys. Rev. B* **2011**, 83 (3). DOI: 10.1103/PhysRevB.83.035410.
- (46) Newberg, J. T.; Starr, D. E.; Yamamoto, S.; Kaya, S.; Kendelewicz, T.; Mysak, E. R.; Porsgaard, S.; Salmeron, M. B.; Brown, G. E.; Nilsson, A.; Bluhm, H. Formation of hydroxyl and water layers on MgO films studied with ambient pressure XPS. *Surf. Sci.* **2011**, 605 (1–2), 89–94.
- (47) Bluhm, H. Photoelectron spectroscopy of surfaces under humid conditions. *J. Electron Spectrosc. Relat. Phenom.* **2010**, 177 (2–3), 71–84.